

# A High-Speed Efficient 220-GHz Spatial-Orthogonal ASK Transmitter in 130-nm SiGe BiCMOS

Chen Jiang, *Student Member, IEEE*, Andreia Cathelin, *Senior Member, IEEE*,  
and Ehsan Afshari, *Senior Member, IEEE*

**Abstract**—Wireless communication using terahertz/sub-terahertz band can alleviate the spectrum scarcity in conventional RF bands and satisfy the drastically expanding demands for capacity. In this paper, a spatial-orthogonal ASK transmitter architecture is presented. The self-sustaining oscillator-based transmitter architecture has an ultra-compact size and excellent power efficiency. With the proposed high-speed constant-load switch, significantly reduced modulation loss is achieved. Using polarization diversity and multi-level modulation, the throughput is largely enhanced. Array configuration is also adopted to enhance the link budget for higher signal quality and longer communication range. Fabricated in a 130-nm SiGe BiCMOS technology, the transmitter achieves an EIRP of 21 dBm and dc-to-THz-radiation efficiency of 0.7% in each spatial channel. A 24.4-Gb/s total data rate over a 10-cm communication range is demonstrated. With an external Teflon lens system, the demonstrated communication range is further extended to 52 cm. Compared with prior art, the proposed transmitter shows much higher power efficiency.

**Index Terms**—BiCMOS, communication, compact design, constant-load switch, data rate, efficiency, EIRP, polarization diversity, SiGe, spatial-orthogonal ASK, sub-terahertz, terahertz, transmitter.

## I. INTRODUCTION

THE demand for wireless communication throughput is expanding drastically, however, the spectrum resources are becoming more and more limited in conventional RF bands. On the other hand, vast unallocated spectrum exists in terahertz/sub-terahertz range, which can provide ultra-wide bandwidth for high-speed communication. Compared with the broadcasting of conventional RF frequencies, the line-of-sight nature also provides better security. Integrating terahertz/sub-terahertz communication systems onto silicon is highly desired for smaller size and lower cost, however, many challenges exist. First of all, signal generation efficiency in this range is still low and modulation circuits normally introduce

Manuscript received November 10, 2016; revised January 15, 2017 and February 28, 2017; accepted May 3, 2017. Date of publication June 7, 2017; date of current version August 22, 2017. This paper was approved by Associate Editor Hossein Hashemi. This work was supported by the Army Research Laboratory and by Army Research Office. (*Corresponding author: Chen Jiang*.)

C. Jiang and E. Afshari are with the Department of Electrical and Computer Engineering, Cornell University, Ithaca, NY 14853 USA, and also with the Department of Electrical Engineering and Computer Science, University of Michigan, Ann Arbor, MI 48109 USA (e-mail: cj342@cornell.edu).

A. Cathelin is with STMicroelectronics, 38920 Crolles, France.

Color versions of one or more of the figures in this paper are available online at <http://ieeexplore.ieee.org>.

Digital Object Identifier 10.1109/JSSC.2017.2702007

large loss. The lack of good power amplifiers also limits the output power of a transmitter. On the receiver side, lack of high-performance low-noise amplifiers causes poor noise performances. Fortunately, due to the small wavelength, antenna arrays can be implemented on chip to significantly enhance the antenna gain to improve the link budget [1].

Recently, terahertz/sub-terahertz communication systems have been demonstrated. In [2], a 210-GHz fundamental frequency transceiver is presented. Due to the limited performance of the power amplifier and the low-noise amplifier, the achieved baseband signal-to-noise ratio (SNR) is less than 14 dB. Several new topologies have also been introduced. In [3] and [4], 240-GHz 16-Gb/s QPSK transmitter and receiver are presented. In the transmitter, a multiplier-last architecture is used, in which signal generation and modulation happen at lower frequency and a frequency tripler pushes the output into sub-terahertz band. However, only limited modulation scheme can be adopted using this scheme and the spectral efficiency is low. The tripler also introduces a large conversion loss. A 300-GHz 32-QAM transmitter is introduced in [5], which uses six frequency channels and a 17.5-Gb/s capacity is achieved in each channel. Cubic mixers are used to mix the second harmonic of LO with IF. Even though massive power combining is used to increase the output power, due to the large conversion loss of the cubic mixer, only  $-14.5$ -dBm output power is achieved while consuming 1.4-W dc power.

Most previous transmitter architectures in this frequency range rely on multiplier-based signal sources [3]–[5], which have relatively lower power efficiency [6]. Meanwhile, large power loss happens in the modulation path, which limits the transmitter output power, efficiency, and communication range (1 cm is demonstrated in [3], wafer probing and waveguide are used in [5]). In this paper, a spatial-orthogonal ASK (SO-ASK) transmitter architecture is proposed. Harmonic oscillators are used for signal generation instead of multiplier-based sources for better power efficiency and higher integration level [7]. A high-speed constant-load modulation switch is also proposed to provide high date rate while significantly reduce the modulation loss. Transmitter array is implemented for better equivalent isotropically radiated power (EIRP). Using polarization diversity, the SO-ASK scheme can double the throughput. Link capacity can be further improved with multi-level modulation. Fabricated in a 130-nm SiGe BiCMOS process, the transmitter achieves a 21-dBm/ch EIRP and a 0.7% dc-to-radiation efficiency in continuous

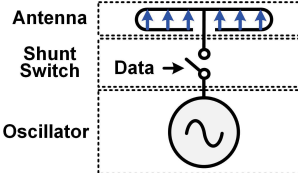


Fig. 1. Oscillator-based OOK transmitter cell structure.

wave (CW) mode. A 24.4-Gb/s total data rate over a 10-cm range is also demonstrated. With an external Teflon lens system, the range is further extended to 52 cm. This paper also shows much higher transmitter efficiency compared with prior art according to our measurement. The proposed system can be used for chip-to-chip communication and short-range ultra-fast device-to-device data exchange. With external collimating lens system to extend the communication range, it also has the potential to be used for future high-speed in-door point-to-point communication.

In Section II, the principle and analysis of the proposed SO-ASK transmitter architecture are discussed. The design details of the high-speed efficient 220-GHz SO-ASK transmitter are given in Section III. The experimental results of the transmitter prototype are presented in Section IV. Finally, a performance summary and comparison with some state-of-the-art terahertz/sub-terahertz communication systems as well as a brief conclusion are given in Section V.

## II. PRINCIPLE AND ANALYSIS OF THE PROPOSED SPATIAL-ORTHOGONAL ASK TRANSMITTER ARCHITECTURE

Generation of terahertz/sub-terahertz power on silicon is relatively inefficient, consequently, it is desired to make full use of the generated power. In this paper, we seek to maximize the signal generation efficiency while minimize the loss in the modulation. Besides, compact design is desired to facilitate array configuration for higher EIRP and better link budget.

### A. Principle of the Spatial-Orthogonal ASK Transmitter

In sub-terahertz/terahertz frequency range, signal modulation can be very lossy. For example, in [3], with 5-dBm LO power, the 80-GHz QPSK modulator can provide only  $-5$ -dBm output power. Adding the  $\sim 12$ -dB conversion loss of the final stage 240-GHz tripper, significant loss is associated with the modulation. For the cubic mixer in [5], with 5-dBm LO power at 97 GHz, the 300-GHz output power is below  $-15$  dB. For better transmitter performance, minimizing the modulation loss is critical. Shown in Fig. 1 is an oscillator-based OOK transmitter. Compared with multiplier-based signal sources that are widely used in previous architectures, oscillators are more power efficient [6]. It is also self-sustaining, which means no high frequency input is needed and higher integration level can be achieved [7]. It will be shown in Section III that, with the proposed high-speed constant-load modulation switch, the power utilization ratio (difference of the percentage of power reaches the antenna port between switch “ON” and “OFF”) achieved is

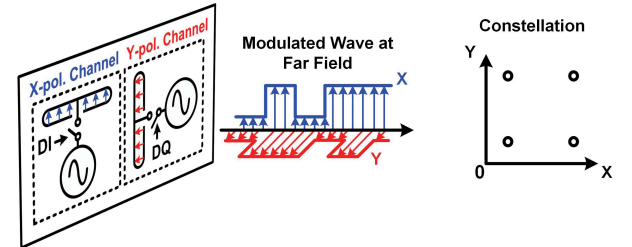


Fig. 2. Principle of the SO-ASK modulation based on polarization diversity and the equivalent constellation plot.

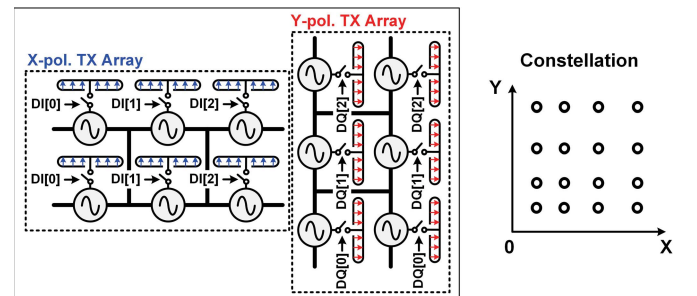


Fig. 3. Principle of the four-level SO-ASK transmitter with  $2 \times 3$  array configuration inside each channel as well as the equivalent constellation plot.

more than 60%. This corresponds to a modulation loss of only  $\sim 2$  dB, which means the signal power generated by the oscillator is well utilized and much higher RF output power can be generated. The structure is also very compact, which facilitates the array configuration. However, there are two obvious drawbacks: 1) the incoherent operation will cause lower receiver sensitivity and 2) the simple modulation scheme provides limited spectral efficiency. Details about the first drawback will be discussed in Section II.B. To compensate the second drawback, polarization diversity can be utilized. It has been shown that two orthogonal polarization states of planar waves can support two separate information channels [8]. As shown in Fig. 2, two transmitter cells with linearly polarized antennas are placed perpendicular to each other. With the two spatial orthogonal channels, the capacity is doubled. If the information in the  $X$ - and  $Y$ -polarized channels is combined, the constellation plot in Fig. 2 is formed. To further increase the spectral efficiency and capacity, multi-level ASK modulation can be implemented inside each spatial channel. As shown in Fig. 3, the transmitter has a  $2 \times 3$  array in each channel. With thermometer coding for  $DI[0:2]$  and  $DQ[0:2]$ , a four-level SO-ASK modulation is realized with constellation plot shown in Fig. 3. This scheme further doubles the capacity. Besides, with power combining and higher antenna gain obtained with the array, larger transmitter EIRP is achieved. In summary, this transmitter architecture can achieve high output power, excellent power efficiency as well as good data rate with simpler implementation and small chip area.

### B. Link Budget Analysis and Comparison

The proposed SO-ASK transmitter architecture can significantly reduce the modulation loss, hence achieving higher

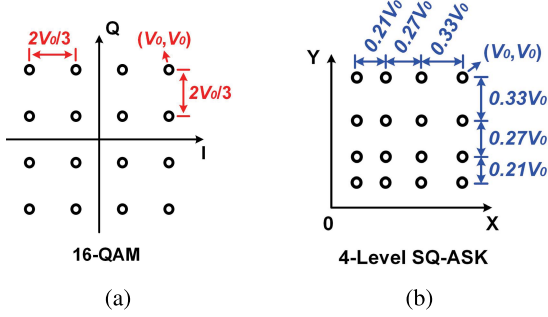


Fig. 4. Constellation plots of (a) typical 16-QAM and (b) proposed four-level SO-ASK.

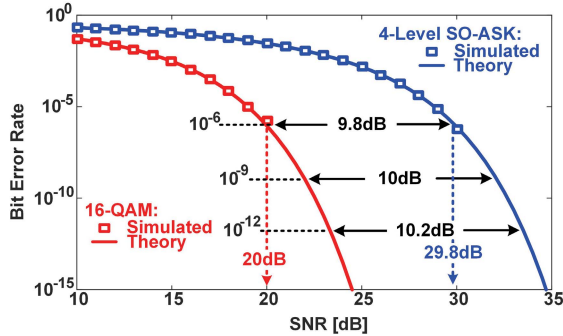


Fig. 5. BER analysis of the 16-QAM and the proposed four-level SO-ASK.

output power and EIRP. However, as mentioned previously, the incoherent operation requires higher transmitter power to compensate the lower receiver sensitivity in order to maintain the same system performance. Fortunately, the disadvantage of incoherent operation becomes much less significant in communication systems due to the high SNR requirement as well as the high noise floor caused by the large bandwidth. On the other hand, higher transmitter EIRP benefited from the lower modulation loss and easier array configuration due to the simpler and more compact structure can significantly improve the system link budget. To show this point more clearly, a comprehensive system performance comparison between a typical 16-QAM and the proposed four-level SO-ASK modulation scheme is performed.

Shown in Fig. 4 are the constellation plots of the typical 16-QAM and the four-level SO-ASK. Due to the directivity of the antenna array slightly changes with turning on different numbers of transmitter cells, the constellation of the four-level SO-ASK has a little distortion. Fig. 4(b) is drawn according to simulation. Based on the constellations, theoretical calculation and MATLAB simulation of bit error rates (BERs) under different SNRs are performed for both cases, with results shown in Fig. 5. The results are obtained with the following assumptions: 1) AWGN channel model [9]; 2) Gray code [10] is used in bit mapping in both schemes; and 3) all the symbols have equal probability. It shows that, for a reasonable BER range ( $<10^{-6}$ ), the proposed SO-ASK scheme needs around 10 dB higher SNR to achieve the same BER. This inferior performance stems from the crowded and slightly distorted constellation in Fig. 4(b). For a target BER of  $10^{-6}$ ,

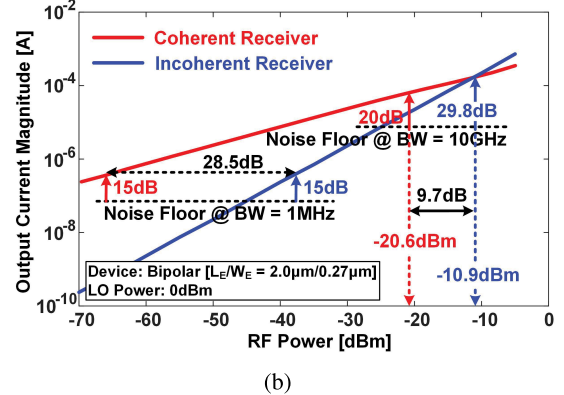
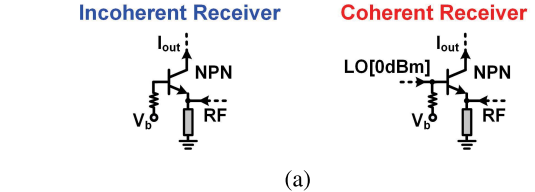


Fig. 6. Receiver sensitivity analysis of the coherent 16-QAM system and the proposed incoherent four-level SO-ASK system. (a) Bipolar transistor configured as both coherent receiver front end and incoherent receiver front end. (b) Sensitivity simulation results.

the minimum SNR required for both cases are 20 and 29.8 dB, respectively. To find out how this disadvantage will affect the receiver sensitivity, circuit level simulations are performed. The same bipolar transistor from the STMicroelectronics 130-nm SiGe BiCMOS technology with emitter length and width of 2 and  $0.27\ \mu\text{m}$ , respectively, is used to configure the receiver front end for both modulation schemes, as shown in Fig. 6(a). The simulation is performed at RF frequency of 220 GHz. For the SO-ASK, an incoherent power detector is enough. For the 16-QAM, the transistor is configured into a mixer with RF power injected from the emitter and a 220.1-GHz LO with 0-dBm power pumped into the base. The simulated output current magnitude with different input RF powers is shown in Fig. 6(b). The noise floor is the rms current noise derived by integrating the output collector noise current inside the assumed bandwidth. In narrow-band applications, such as imaging and spectroscopy, coherent sensing significantly enhances the receiver sensitivity [11], [12]. As shown in Fig. 6(b), with 1-MHz bandwidth and minimum SNR of 15 dB, the sensitivity difference between the coherent and incoherent receivers is almost 30 dB. However, in communication systems, large bandwidth is normally required, which significantly reduces this sensitivity difference: with a bandwidth of 10 GHz and a targeted BER of  $10^{-6}$  (corresponding to minimum SNR of 20 and 29.8 dB for the two cases), the sensitivity difference is only 9.7 dB. This difference will further shrink if larger bandwidth is required for higher capacity or higher SNR is required for better BER. It is noteworthy that, in the previous comparison, we assume that fundamental LO is applied, however, in real scenario, fundamental LO with high power is hard to obtain and subharmonic mixing is often used [5], [11]. In this case, the sensitivity difference will also significantly shrink. Also, as discussed previously,

in the SO-ASK transmitter, the switch-based ASK modulation can achieve much lower modulation loss (10 dB or more), which can compensate the sensitivity disadvantage caused by incoherent operation.

It is mentioned previously that array configuration can effectively increase the transmitter EIRP and benefit the link budget. There are two ways to configure the array: 1) replicate just the antenna and use the transmitter to feed the antenna array and 2) replicate the whole transmitter cell to form a transmitter array. In theory, with an array size of  $N$ , transmitter array can produce  $N^2$  larger EIRP, while antenna array only improves the EIRP by  $N$ . For previous transmitter architectures, there are two obstacles for implementing transmitter array: 1) the high frequency LO distribution with acceptable delay/phase mismatch is complicated to achieve and 2) the large physical size limits the smallest antenna distance and grating lobes may degrade the EIRP enhancement. Even for implementing antenna array, RF signal distribution and impedance matching can be complicated and lossy when array size is large. However, with much more compact size and no need for LO distribution, the proposed SO-ASK system is very convenient to be replicated to form large transmitter arrays. Besides, for the SO-ASK system, only incoherent receiver is required. Again, with compact size and no issue of LO distribution, incoherent receivers are also much easier to form arrays to increase the receiver antenna directivity and further enhance the system performance.

It is worth mentioning that, even though there are many other devices and topologies for implementing coherent and incoherent receivers, the results in Fig. 6(b) represent a typical trend. Intuitively, coherent systems can offer higher sensitivity due to LO power is normally much higher than the received RF power. However, in communication systems, with larger input power requirement caused by larger bandwidth and higher minimum SNR, the difference between RF and LO power shrinks, so does the sensitivity difference. Consequently, the qualitative conclusions drawn here are true for not only the implementation shown in Fig. 6(a) but also for most other similar cases.

In summary, the proposed SO-ASK transmitter has the potential to achieve better system link budget (meaning higher signal quality or longer communication range) as well as similar data rate and spectral efficiency with lower system complexity, smaller area, and higher power efficiency. Also, with compact size and no need for high-frequency LO distribution, it is highly scalable into larger arrays, which can help achieving longer communication range or more levels of modulation for higher data rate.

### III. DESIGN OF THE 220-GHz SPATIAL-ORTHOGONAL ASK TRANSMITTER

The proposed four-level SO-ASK transmitter has two perpendicular  $2 \times 3$  transmitter arrays as shown in Fig. 3. Each transmitter cell is composed of a harmonic oscillator, a compact slot antenna, and a constant-load high-speed switch. Next, design details of the circuit blocks are described.

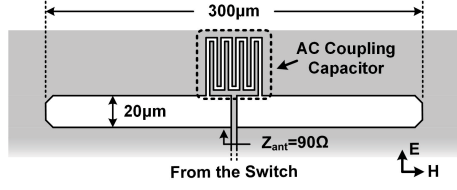


Fig. 7. 220-GHz compact slot antenna.

#### A. Slot Antenna

To create spatial orthogonal channels, the antenna needs to be linearly polarized. For a high data rate, a wide antenna bandwidth is required. A compact design is also desired for easier array configuration and lower cost. In this paper, a slot antenna shown in Fig. 7 is adopted. The antenna length is 300  $\mu\text{m}$ , which is around half wavelength at 220 GHz. The width is tuned to 20  $\mu\text{m}$  for a suitable input impedance. A custom-designed ac-coupling capacitor is used to separate the dc of the antenna input port from the ground. According to HFSS simulation, bandwidth of the antenna is more than 30% ( $\sim$ 68 GHz near 220 GHz), which is wide enough for the transmitter. The antenna input impedance and efficiency is 90  $\Omega$  and 63%, respectively. It also has a small size, which is suitable for array configuration. The simulated radiation patterns of the slot antenna and a  $2 \times 3$  array formed with this antenna are shown in Fig. 8. For the array, a broadsided directivity is simulated to be 15.9 dBi and the cross polarization is more than 40 dB lower than the co-polarization, which ensures very good isolation between the two channels.

#### B. Harmonic Oscillator

The oscillator is the most power hungry part in the transmitter, hence, its generated power and efficiency is of great importance. For array configuration, a compact design is also desired. Since the targeted frequency 220 GHz is close to the device  $f_{\max}$  in this process ( $f_{\max} = 280$  GHz [13]), harmonic oscillator is used. For optimal output power, harmonic generation efficiency as well as compact size, the return-path-gap-based self-feeding oscillator structure as shown in Fig. 9 is used. Detailed working principle and design of this oscillator structure have been introduced in our previous work [7], [14]. The self-feeding structure can provide the transistors with optimum collector-to-base phase shift for optimal harmonic generation; the return-path gap structure can provide the desired collector-base isolation at the second harmonic to eliminate the self-power-cancellation/loading effect; the return-path gap structure also naturally separates the dc of the transistor base and collector for optimal biasing. The generated second harmonic power is sent to the switch for modulation. Two additional ports at the two sides of the self-feeding lines are for synchronization with neighboring oscillators in the transmitter array. According to simulation, under a supply voltage of 2 V and a bias current of 15 mA for each transistor, the optimum load of the oscillator is 14  $\Omega$ , and each of the oscillators can generate 1.4 mW power at 220 GHz with a dc-to-terahertz efficiency of 2.5%. In principle, frequency tuning is not important in this system, however, it is worth mentioning that, based on parasitic tuning [7], the oscillator can achieve a total tuning range of around 10%.

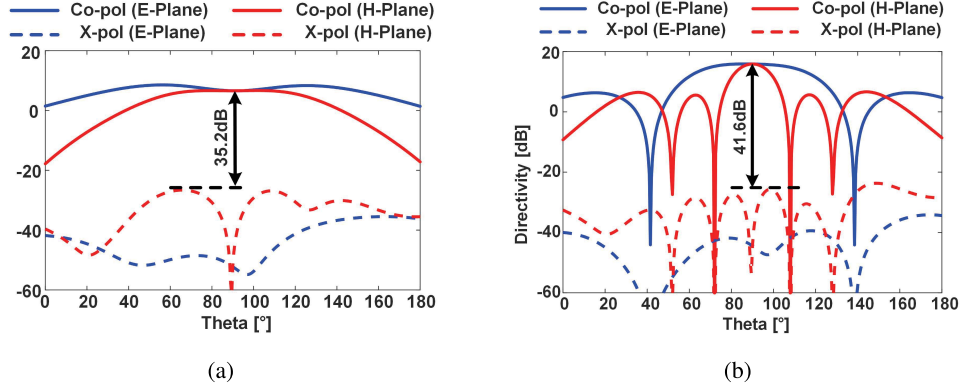


Fig. 8. Simulated antenna directivity of (a) slot antenna and (b) 2×3 array.

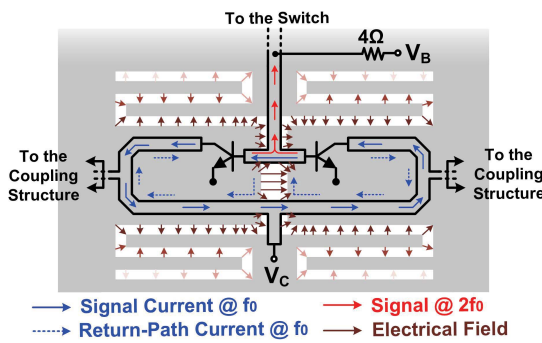


Fig. 9. Schematic of the return-path-gap-based self-feeding harmonic oscillator.

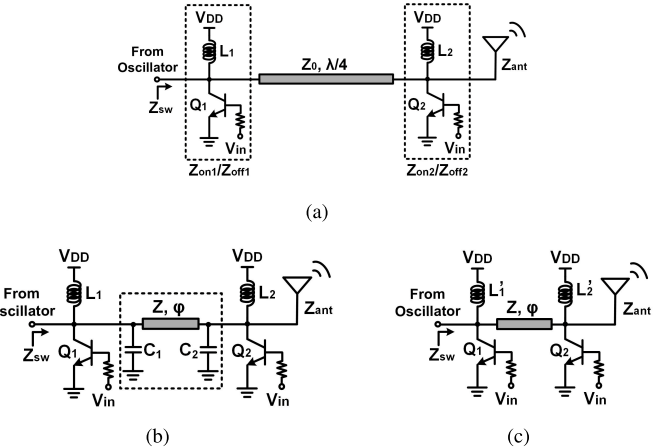
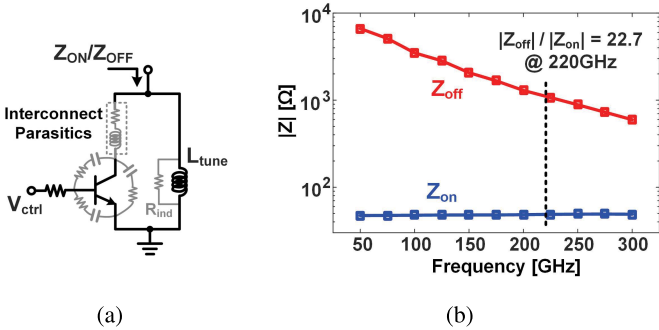


Fig. 11. Evolving of the constant-load high-speed modulation switch. (a) Initial form. (b) After size shrinking. (c) After tuning out of the capacitors.

Fig. 10. Shunt switch based on a bipolar transistor. (a) Schematic. (b) Simulated ON/OFF switch impedances at different frequencies (assume ideal L<sub>tune</sub>).

### C. Constant-Load High-Speed Modulation Switch

Designing a high-performance switch at this frequency is challenging. It needs to have ultra-fast switching speed, low insertion loss and good isolation when turned off. In this design, shunt switch topology is used for its low insertion loss. Shown in Fig. 10(a) is a bipolar transistor used as a shunt switch. With the parasitic capacitance tuned out with the shunt inductor L<sub>tune</sub>, the impedance seen from the collector node is near pure resistive both when the transistor is “ON” and “OFF.” With ideal shunt inductor L<sub>tune</sub>, the simulated “ON” and “OFF” impedances of the transistor (Z<sub>on</sub> and Z<sub>off</sub>) are shown in Fig. 10(b). As we can see, Z<sub>ON</sub> remains relatively constant while Z<sub>OFF</sub> drops quickly with frequency. This is caused by

the quality factor of the parasitic capacitances of the transistor decreases with frequency, which causes a higher leakage of signal from the transistor collector to the emitter, and thus smaller Z<sub>OFF</sub>. At 220 GHz, the ON/OFF ratio of the shunt switch |Z<sub>OFF</sub>/Z<sub>ON</sub>| is 22.7. It is worth mentioning that, in reality, due to the limited quality of passive on-chip components, the parallel parasitic resistance of L<sub>tune</sub> [R<sub>ind</sub> in Fig. 10(a)] degrades the switch ON/OFF ratio to |(Z<sub>OFF</sub> + R<sub>ind</sub>)/(Z<sub>ON</sub> + R<sub>ind</sub>)|. At 220 GHz, with L<sub>tune</sub> implemented with G-CPW transmission line, the simulated ON/OFF ratio drops to around 10.

For ultra-fast switching, the switch needs to have a constant input impedance so that the oscillator is not disturbed and there is no need to wait for it to settle until the next switching. In this paper, a constant-load shunt switch is proposed. As shown in Fig. 11(a), the switch is composed of two shunt bipolar switches and a quarter-wave length transmission line. When both switches are “ON” or “OFF,” the switch input impedances Z<sub>sw,ON</sub> and Z<sub>sw,OFF</sub> are

$$Z_{sw,ON} = \frac{Z_{ON1}Z_0^2}{Z_0^2 + Z_{ON1}Z_{ON2}}, \quad Z_{sw,OFF} = \frac{Z_{OFF1}Z_0^2}{Z_0^2 + Z_{OFF1}Z_{OFF2}} \quad (1)$$

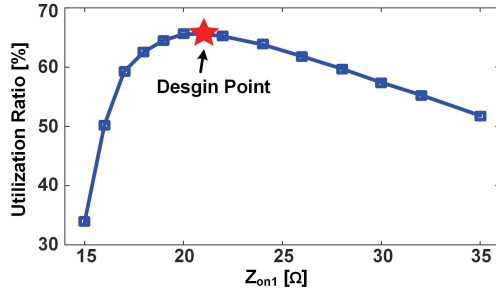


Fig. 12. Simulated terahertz power utilization ratio versus  $Z_{ON1}$ . The design point is chosen near the peak of the curve.

in which,  $Z_{ON1}$ ,  $Z_{OFF1}$ ,  $Z_{ON2}$ , and  $Z_{OFF2}$  are the “ON” and “OFF” impedances of the two bipolar shunt switches,  $Z_0$  is the characteristic impedance of the quarter-wave line. In order to have the switch input impedance to remain constant near the optimum load of the oscillator ( $Z_{opt} = 14 \Omega$ ), the following equation needs to be satisfied:

$$\frac{Z_{ON1}Z_0^2}{Z_0^2 + Z_{ON1}Z_{ON2}} = \frac{Z_{OFF1}Z_0^2}{Z_0^2 + Z_{OFF1}Z_{OFF2}} = Z_{opt}. \quad (2)$$

If ON/OFF ratios of both switches are assumed to be 10, given a  $Z_{ON1}$ , with (2), all other parameters can be calculated. The power utilization ratio is defined as the difference of percentage of power sent to the antenna when the switch is “ON” and “OFF.” With different  $Z_{ON1}$ , power utilization ratio of the switch is simulated as shown in Fig. 12. For optimal power utilization ratio and room for process variation,  $Z_{ON1}$  is chosen to be  $21 \Omega$ .

It has been mentioned previously, compact design is preferred for array configuration. In the switch structure shown in Fig. 11(a), the quarter-wave line takes large area. To reduce the size, as shown in Fig. 11(b), the quarter-wave line can be replaced with a much shorter line section and two lumped capacitors [16], with

$$Z = Z_0/\sin\varphi, \quad \omega C_1 = \omega C_2 = (1/Z_0)\cos\varphi \quad (3)$$

where  $Z$  and  $\varphi$  are the impedance and electrical length of the transmission line section, and  $C_1$  and  $C_2$  are the values of the two lumped capacitors. Capacitor  $C_1$  and  $C_2$  can then be tuned out with part of  $L_1$  and  $L_2$  as shown in Fig. 11(c). The new inductors  $L'_1$  and  $L'_2$  can be calculated as

$$\omega L'_1 = \omega L_1 - \frac{1}{\omega C_1}, \quad \omega L'_2 = \omega L_2 - \frac{1}{\omega C_2}. \quad (4)$$

Comparing the switches in Fig. 11(a) and (c), beside the smaller size of the quarter-wave length line, there is an additional benefit. According to (4), the inductors  $L'_1$  and  $L'_2$  are smaller than  $L_1$  and  $L_2$ . Since the quality factor of passive components with similar implementation does not change much at a certain frequency, the parallel parasitic resistance [ $R_{ind}$  in Fig. 10(a)] of  $L'_1$  and  $L'_2$  is larger, which means a better switch ON/OFF ratio. This, along with lower passive loss due to shorter lines, helps to achieve a higher power utilization ratio.

Final structure of the constant-load high-speed shunt switch is shown in Fig. 13(a). The lossy Via connections from

TABLE I  
STATIC SIMULATION RESULTS OF THE CONSTANT-LOAD SWITCH WITH 90-Ω ANTENNA LOAD AT 220 GHz

	$Z_{off}/Z_{on}$	Data	“1”	“0”
Switch ' $Q_1$ '	9.7	$Z_{sw}$	$(14.1 + j0.2) \Omega$	$14.0 \Omega$
Switch ' $Q_2$ '	9.4	$P_{out}/P_{osc}$	12.1%	75.6%

the transistors to transmission lines will lower the switch ON/OFF ratio and increase the insertion loss. To alleviate this impact,  $TL_1 - TL_3$  are implemented on the second top metal M5 instead of the top metal M6 (M5 and M6 have the same thickness of  $3 \mu m$  in this process). To reduce time constant for faster switching, biasing resistors in Fig. 11(c) are replaced with transmission lines  $TL_4$  and  $TL_5$ . To maintain high impedance at the base of  $Q_1$  and  $Q_2$  for low switch insertion loss,  $TL_4$  and  $TL_5$  are near quarter-wave length to transform the low digital buffer output impedance into a high impedance. Size of the two digital buffers is chosen to minimize the input data delay mismatch between the two paths. A duty-cycle control is also implemented to shape the input waveform. The drawback of the size shrinking described previously is the reduction of the bandwidth. However, according to the S-parameter simulation results shown in Fig. 13(b), the achieved bandwidth is still more than 40 GHz, which is wide enough for the system. At frequency point of 220 GHz, the simulated switch performances are given in Table I. The switch input impedance remains around  $14 \Omega$  during switching, and 63.5% of the input power is utilized. Fig. 14(a) shows the simulated transient oscillator output waveform while the switch toggles. Due to the input impedance of the shunt switch seen by the oscillator is not exactly constant, there will be a small disturbance of the oscillation during the switching. However, since the recover time is only about 50 ps, ultra-fast switching can still be achieved. Fig. 14(b) and (c) shows the simulated transient power delivered to the antenna with 5 and 8 GHz sinusoidal waves as data input, which show a switching speed higher than 8 GHz. This means that the achievable data rate with the four-level SO-ASK transmitter can exceed 64 Gb/s.

#### D. Coupling of the Transmitter Cells

To obtain higher EIRP and functionality of multi-level modulation, each spatial channel has a  $2 \times 3$  transmitter array as shown in Fig. 3. Inside each array, all the oscillators need to be synchronized for coherent power combining. To achieve this, a coupling network shown in Fig. 15 is designed. To explain how the coupling network works, a simpler case with four oscillators shown in Fig. 16(a) is discussed. Relative to  $OSC_1$ , its neighbors  $OSC_2$  and  $OSC_3$  can be either in-phase or out-of-phase. Consequently, there are four primary modes, and combination of the four modes can form any arbitrary phase relation among them. In these modes, center points A and B in Fig. 16(a) present either virtual open or virtual ground, and the impedance seen by  $OSC_1$  under each mode can be determined as shown in Table II. The results are also plotted on a Smith chart for more intuitive comparison as shown in Fig. 16(b). As we

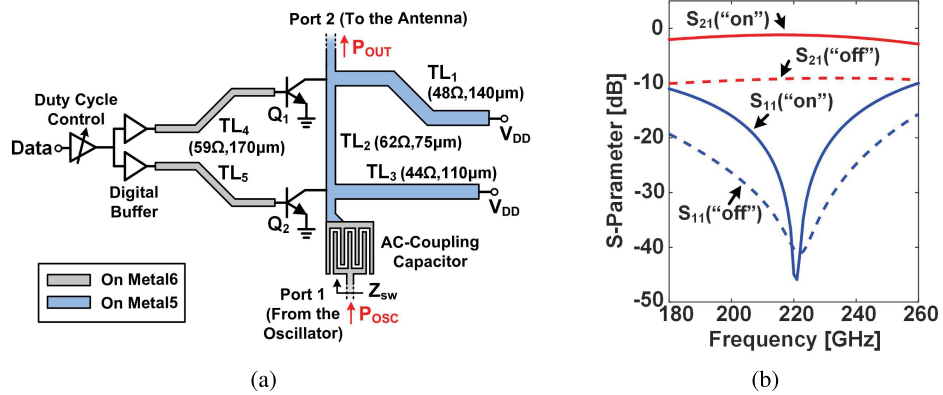


Fig. 13. Final design of the constant-load high-speed modulation switch. (a) Schematic. (b) S-parameter simulation.

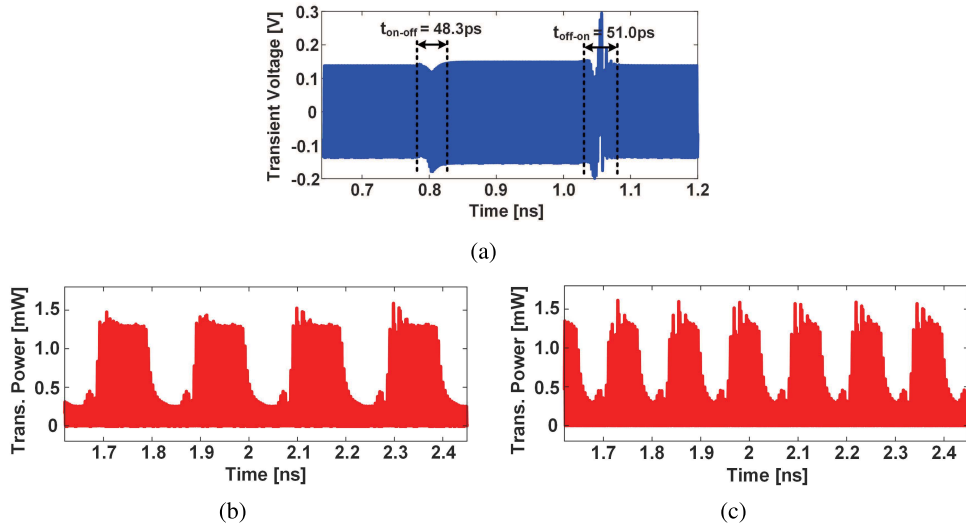


Fig. 14. Dynamic simulation results of the constant-load high-speed modulation switch. (a) Oscillator output waveform while switching, as well as transient power at the output of the switch with input clock rate of (b) 5 GHz and (c) 8 GHz.

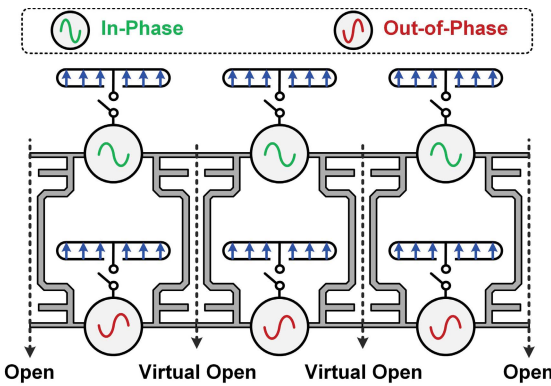


Fig. 15. Coupling network among the 2×3 transmitter array.

can see, in three of the four primary modes, oscillators see low impedances, which are equivalent to large shunt capacitance or small shunt inductance, and the oscillation will be disturbed. This means that the three modes are not well supported with the given structure. Only when OSC<sub>2</sub> is in-phase and OSC<sub>3</sub> is out-of-phase, the oscillators see a large impedance and the oscillation is not affected, which makes it the dominant mode. For the same reason, in the 2 × 3 array

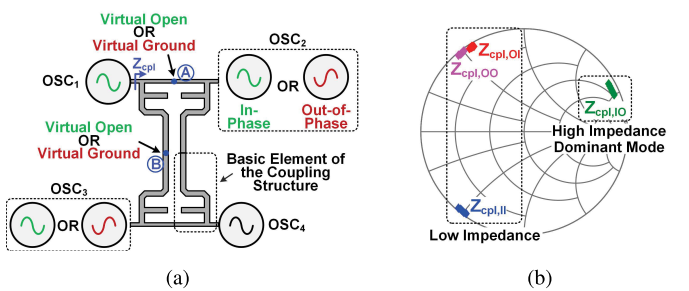


Fig. 16. Analysis of the coupling network in the transmitter array. (a) Four-oscillator case. (b) Simulated impedances seen by the oscillators in the four modes.

shown in Fig. 15, the fundamental signals of the oscillators are in-phase within the upper row and the lower row in steady state, but between the two rows, they are out-of-phase. As a result, the central line of the two coupling structures among the transmitter cells present virtual open, as shown in Fig. 15. If the two sides of the whole array are left open, the symmetry of the whole array is well preserved. Since the oscillators in the array are either in-phase or out-of-phase with each other, their second harmonic are all in-phase and power combining is obtained. Also, as mentioned before, the coupling

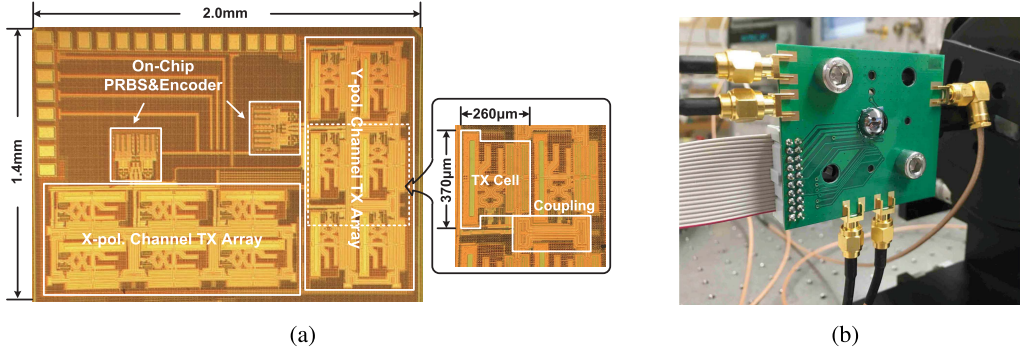


Fig. 17. Transmitter chip. (a) Die photograph. (b) PCB photograph.

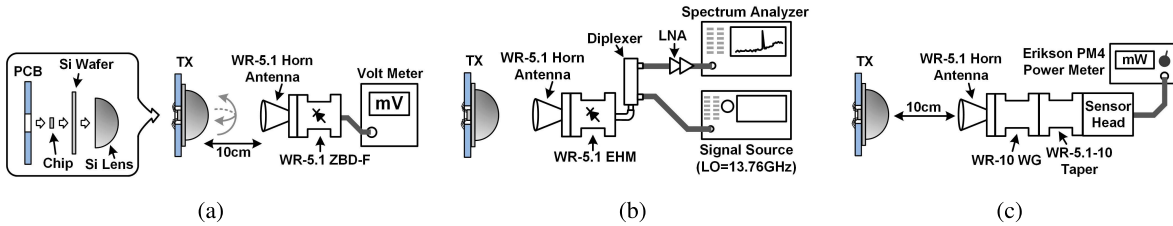


Fig. 18. Measurement setups. (a) Radiation pattern setup. (b) Frequency/spectrum setup. (c) Power measurement setup.

TABLE II  
IMPEDANCE OF THE COUPLING NETWORK UNDER DIFFERENT MODES

$\text{OSC}_2$	In-Phase	Out-of-Phase
In-Phase	$Z_{\text{cpl},II}$ ( $0.7 - j24.2$ ) $\Omega$	$Z_{\text{cpl},IO}$ ( $36.1 + j230.0$ ) $\Omega$
Out-of-Phase	$Z_{\text{cpl},OI}$ ( $0.7 + j23.6$ ) $\Omega$	$Z_{\text{cpl},OO}$ ( $1.1 + j27.7$ ) $\Omega$

network presents high impedance, consequently, it has almost no loading effect to the oscillators and little power is injected into the structure, which means negligible additional loss.

#### E. On-Chip PRBS Generator and Encoder

For ease of measurement, pseudorandom binary sequence (PRBS) generator and thermometer encoder are included in each spatial channel. With clock signal provided off-chip, the PRBS can generate two synchronized independent ( $2^7 - 1$ ) pseudorandom sequences. When multi-level function is turned on, the two sequences are fed into the thermometer encoder to provide inputs for the transmitter array. When multi-level is OFF, the thermometer encoder is bypassed, and one sequence is directly used as data input for the whole array.

#### IV. EXPERIMENTAL RESULTS

The proposed SO-ASK transmitter chip is fabricated using the STMicroelectronics 130-nm SiGe BiCMOS process with the chip and PCB photographs shown in Fig. 17. With the ultra-compact design for all the blocks, the size of one transmitter cell is as small as  $370 \mu\text{m} \times 260 \mu\text{m}$ , which is the

smallest wireless terahertz/sub-terahertz transmitter for communication application to the best of our knowledge (around 20 times smaller compared with [3] and 60 times smaller than [5]). In each spatial channel, the  $2 \times 3$  transmitter array has an area of  $1.3 \text{ mm} \times 0.6 \text{ mm}$ . The whole chip dimension is  $1.4 \text{ mm} \times 2.0 \text{ mm}$ .

#### A. Performance Characterization of the Spatial-Orthogonal ASK Transmitter

The transmitter radiates from the backside of the silicon chip, in order to eliminate the lossy substrate wave, as shown in Fig. 18(a), a high-resistivity hemispherical silicon lens with 10-mm diameter is attached. It is worth mentioning that the chip is located close to the spherical center of the lens, as a result, it has negligible beam collimating effect [17], [32]. For ease of packaging and silicon chip alignment, a silicon wafer ( $250 \mu\text{m}$  thick) is placed between the transmitter chip and the silicon lens [11], [14]. The radiation pattern measurement setup is shown in Fig. 18(a). The transmitter chip is fixed on a rotary stage, which can rotate in both azimuth and elevation directions. The VDI zero-bias detector (ZBD-F) and the linear polarized conical horn antenna are used to measure the power in each direction. The measured radiation patterns in both spatial channels are shown in Fig. 19. Since the same transmitter array is used in both  $X$ - and  $Y$ -polarized channels with  $90^\circ$  rotation, the radiation pattern is quite similar. The measured directivity is 16.4 and 16.3 dBi, respectively.

In the spectrum measurement, as shown in Fig. 18(b), the VDI even harmonic mixer (EHM) is used to mix the received signal with the 16th harmonic of the 13.76-GHz LO provided by the signal source. The downconverted signal is observed on a spectrum analyzer. The measured downconverted signal spectrum with different data inputs is shown in Fig. 20. The

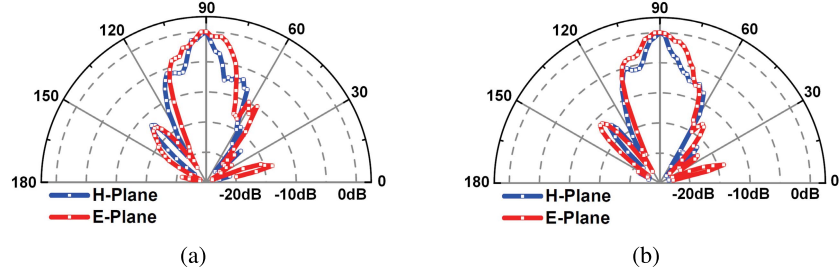


Fig. 19. Measured radiation pattern of (a) X-polarized channel and (b) Y-polarized channel.

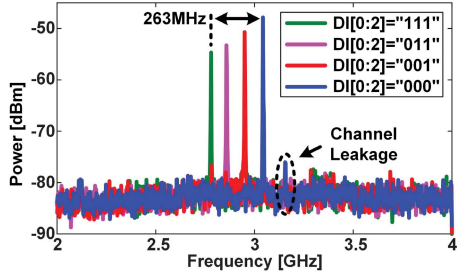


Fig. 20. Measured spectrum of the downconverted transmitter radiation with different data inputs.

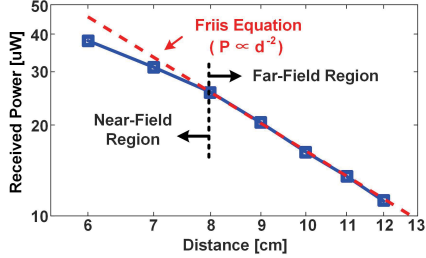


Fig. 21. Received power measured by the calorimeter at different distances from the transmitter chip. After 8 cm, the results agree with the Friis equation well.

CW frequency is measured to be 217.1 GHz and the frequency variation is kept within 0.26 GHz while different input data applied, which proves the effectiveness of the constant-load modulation switch. Fig. 20 also shows the channel leakage (Y-polarized channel configured in CW mode with peak output power) is around 30 dB lower, which demonstrates a very good isolation between the two channels.

The power measurement setup is shown in Fig. 18(c), in which the PM4 calorimeter is used for better precision. For accurate measurement results, the far-field condition needs to be satisfied and standing wave effect must be avoided. Since the horn antenna has a aperture diameter  $D_{\text{horn}}$  of 8.4 mm [18], the silicon lens has a height  $H_{\text{Lens}}$  of 5 mm and the silicon wafer thickness  $T_{\text{wafer}}$  is 250  $\mu\text{m}$ , the far-field distance can be calculated as [17], [19]

$$D_{\text{far-field}} = \frac{2D_{\text{horn}}^2}{\lambda_0} - (\sqrt{\epsilon_{\text{Si}}} - 1)(H_{\text{Lens}} + T_{\text{wafer}}) \approx 8.9 \text{ cm}. \quad (5)$$

To verify this, in our measurement, the distance between the transmitter and the antenna is first changed from 6 to 12 cm, and the received power is measured and shown in Fig. 21.

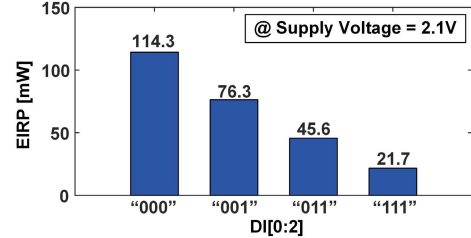


Fig. 22. Measured X-polarized channel output EIRP with different input codes.

The results show that, when the distance is larger than 8 cm, the measurement matches with the Friis equation [20] well, which is close to the theoretical calculation. In the following measurements, a 10-cm distance is chosen. With supply voltage fixed at 2.1 V, the transmitter EIRP of the X-polarized channel under each data input is shown in Fig. 22. As mentioned previously, the numbers are not equally spaced due to the antenna directivity of the transmitter slightly changes with data inputs. This distortion can be compensated with adjusting the output power of the transmitter cells in the array. With data input of "000," the transmitter is set to CW mode with peak output power. Under this mode, the transmitter EIRP and the associated power consumption of the X-polarized channel under different supply voltages are shown in Fig. 23(a). With the results, the total radiated power and dc-to-THz-radiation efficiency can be calculated, as shown in Fig. 23(b). The measured peak EIRP and total radiated power in the X-polarized channel are 21.1 dBm and 3.0 mW, respectively. Thanks to the low insertion loss achieved with the proposed modulation switch, a 0.72% peak dc-to-THz-radiation efficiency is achieved. Similarly, the performance of the Y-polarized channel is also characterized. The peak EIRP, radiated power, and dc-to-THz-radiation efficiency of the Y-polarized channel are 20.9 dBm, 2.9 mW, and 0.7%, respectively, which is very close to the X-polarized channel.

### B. Communication Link Demonstration

To demonstrate the communication link, a conical horn antenna with 21-dBi gain [18] and a ZBD-F with a noise equivalent power (NEP) of 3 pW/ $\sqrt{\text{Hz}}$  and a responsivity of 3000 V/W [21] are configured as the receiver, as shown in Fig. 24. Unfortunately, the ZBD-F is not designed for 50- $\Omega$  load and has an output impedance of 1.07 k $\Omega$ . The large signal loss caused by this impedance mismatch will significantly

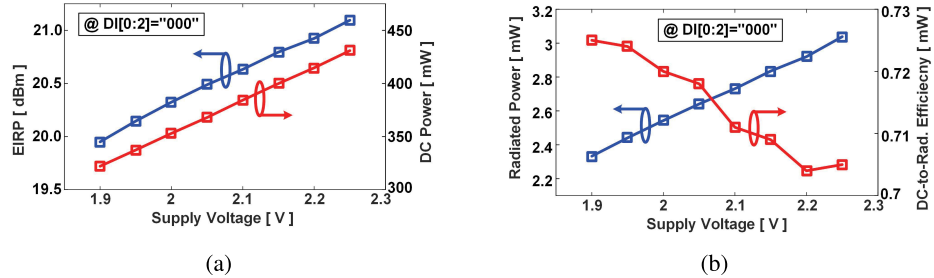


Fig. 23. Measured X-polarized channel. (a) Peak EIRP and the associated power consumption and (b) peak radiated power and the associated dc-to-THz-radiation efficiency at different supply voltages with the input code fixed at “000.”

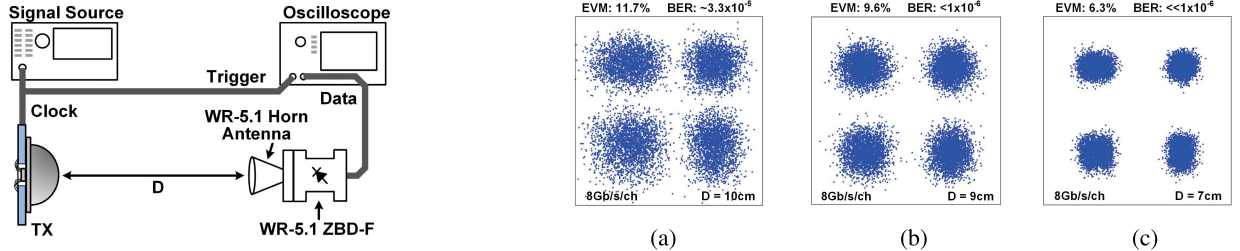


Fig. 24. Communication link experiment setup. A ZBD-F from VDI is used as the receiver.

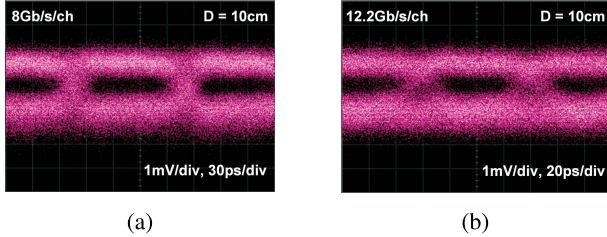


Fig. 25. Measured X-polarized channel eye diagrams with 10-cm communication range and multi-level function turned off. (a) 8 Gb/s/ch. (b) 12.2 Gb/s/ch. Eye opening is largely affected by the 17-dB SNR drop caused by the impedance mismatch between the ZBD-F and the oscilloscope.

increase the noise contribution of the oscilloscope and degrade the overall NEP. With the oscilloscope configured to a 26.5-GHz bandwidth, it has an rms input noise of 0.46 mV [22]. The overall NEP of the receiver can be calculated as [23]

$$\text{NEP}_{\text{RX}} = \sqrt{\text{NEP}_{\text{det}}^2 + \left( \frac{Z_{o,\text{det}} + 50 \Omega}{50 \Omega} \cdot \frac{v_{n,\text{rms}}}{R_{\text{det}}} \right)^2} \frac{1}{\text{BW}} \\ = 21.3 \text{ pW}/\sqrt{\text{Hz}} \quad (6)$$

in which,  $\text{NEP}_{\text{det}}$ ,  $Z_{o,\text{det}}$ , and  $R_{\text{det}}$  are the NEP, output impedance, and responsivity of the ZBD-F;  $v_{n,\text{rms}}$  and  $\text{BW}$  are the rms noise and bandwidth of the oscilloscope, respectively. Compared with the original  $3\text{-pW}/\sqrt{\text{Hz}}$  NEP of the ZBD-F, this impedance mismatch causes a 17-dB SNR drop. This issue can be avoided by inserting a wideband ( $>10$  GHz) low-noise buffer with high input impedance and  $50\Omega$  output impedance between the ZBD-F and the oscilloscope, which is difficult to find in commercial components but very possible to custom design. In our experiment, despite this 17-dB SNR drop, with excellent transmitter EIRP achieved, we are still

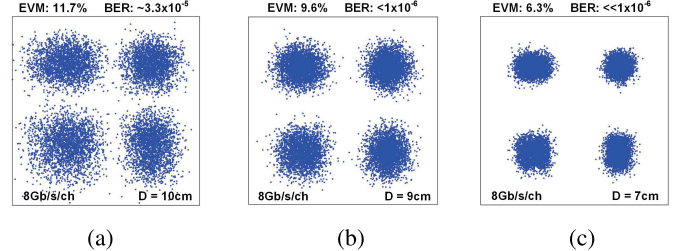


Fig. 26. Measured constellation plots at data rate of 8 Gb/s/ch with different ranges. (a) 10, (b) 9, and (c) 7 cm.

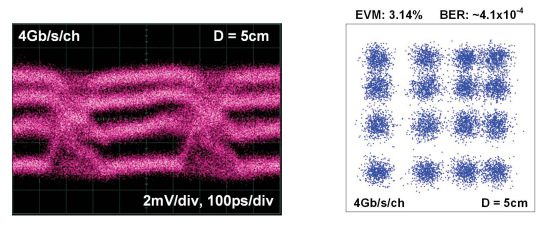


Fig. 27. X-polarized channel measurement results with 5-cm communication range and multi-level function turned on. (a) Eye diagram and (b) constellation at 4 Gb/s/ch. (c) Eye diagram and (d) constellation at 8.4 Gb/s/ch. Eye opening and BER are largely affected by the 17-dB SNR drop caused by the impedance mismatch between the ZBD-F and the oscilloscope.

able to demonstrate the communication link without the buffer. First, with a 10-cm communication range and the multi-level function of the transmitter turned off, the measured eye diagrams of the X-polarized channel are shown in Fig. 25. The Y-polarized channel eye diagrams are very similar, so they are not shown here. With PRBS input clock set to 4 GHz, a total 16-Gb/s data rate is achieved with a BER of  $3.3 \times 10^{-5}$ . With PRBS clock of 6.1 GHz, 24.4-Gb/s capacity is obtained with BER of  $7.2 \times 10^{-5}$ . Implemented with 130-nm CMOS transistors, the PRBS circuit can only work up to a frequency

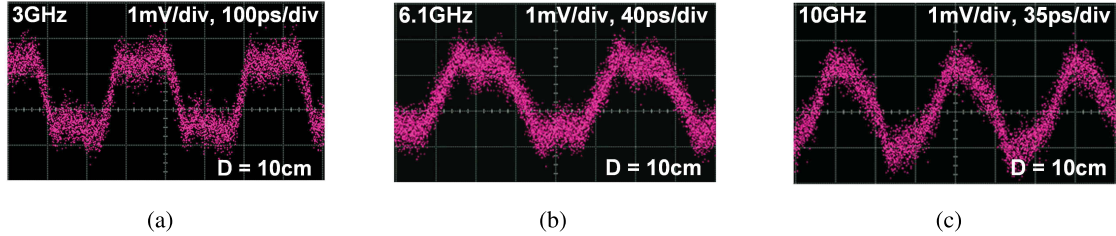


Fig. 28. Single-tone test of the transmitter with input frequency of (a) 3, (b) 6.1, and (c) 10 GHz.

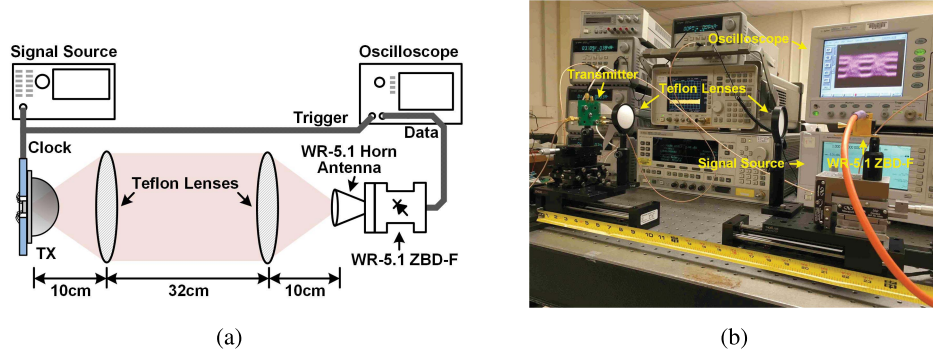


Fig. 29. Teflon lens system experiment setup. (a) Block diagram and (b) photograph of the setup. The extended transmitter to receiver distance is 52 cm, which is limited by the length of the linear tracks.

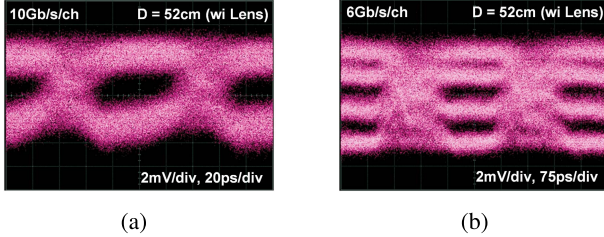


Fig. 30. Measured X-polarized channel eye diagrams with the lens system. (a) With PRBS clock of 5 GHz and multi-level turned off. (b) With PRBS clock of 1.5 GHz and multi-level turned on.

of 6.1 GHz, which limits the highest speed that can be demonstrated. The achieved BER is determined by the power received by the receiver. With a shorter range, larger power can be received, leading to better SNR and BER as shown in Fig. 26. With the limited receiver equivalent NEP, in order to demonstrate the four-level SO-ASK, the communication range is further reduced to 5 cm for a higher SNR. The measurement results are shown in Fig. 27. Beyond 2.1 GHz, the thermometer encoder cannot work properly, consequently, a maximum total data rate of only 16.8 Gb/s is demonstrated. According to Friis equation, by reducing communication range to half, the SNR can increase by 12 dB. However, due to 5 cm has entered the near-field region according to Fig. 21 and the ZBD-F saturates, only  $\sim 7$  dB increase in SNR is obtained compared with the previous 10-cm range.

In previous experiments, the demonstrated data rate is limited by the PRBS and thermometer encoder circuits, while the transmitter itself has a potential for higher speed. To further estimate the transmitter speed, both PRBS and encoder are bypassed and sinusoidal signals are used directly as data inputs. With single-tone frequency sweeping from 1 to 10 GHz, the receiver output amplitude is observed. Fig. 28 gives

the results for 3, 6.1, and 10 GHz, which shows no significant amplitude drop up to 10 GHz. Consequently, the potential modulation speed of the transmitter exceeds 10 GHz. This corresponds to a potential total data rate of at least 40 Gb/s with the multi-level function OFF and at least 80 Gb/s with the multi-level function ON. Due to the 17-dB SNR drop caused by the impedance mismatch between the ZBD-F and the oscilloscope, the demonstrated eye diagram quality, BER, and communication range are all significantly affected. Due to the fact that  $50\ \Omega$  is the standard impedance for commercial high-speed components, in our experiment, the impedance mismatch is difficult to avoid. However, in real applications, using custom-designed baseband circuits with high input impedance, this issue can be eliminated. By de-embedding the 17-dB SNR drop, with the measured transmitter specifications and a targeted BER of  $10^{-6}$ , the proposed transmitter can potentially achieve a calculated communication range of 12.4 and 23.1 cm when the multi-level function ON and OFF, respectively. It is also worth mentioning that, beside the impedance mismatch, the receiver in our measurement is not ideal in two other aspects. First, the ZBD-F 1 dB compression point is only  $-20$  dBm [21], but with the high EIRP of the transmitter, more than  $-10$ -dBm power can be received at a 5-cm range, which will cause the ZBD-F to saturate and affect the SNR. Second, no baseband filter is implemented, which will cause noise to accumulate within the whole 26.5-GHz oscilloscope bandwidth. If a silicon receiver is to be designed, larger device size can be used for higher 1-dB compression point and baseband filter can be implemented to reduce the noise bandwidth. In fact, the state-of-the-art silicon terahertz detectors can achieve an NEP below  $10\text{ pW}/\sqrt{\text{Hz}}$  [25], which is close to the commercial VDI detectors.

The proposed SO-ASK transmitter consumes a total dc power of 0.45 W inside each spatial channel, in which the

TABLE III  
PERFORMANCE SUMMARY AND COMPARISON

Reference	JSSC 2014 [2]	JSSC 2015 [3]	ISSCC 2016 [5]	TMTT 2016 [28]	TMTT 2016 [29]	This Work	
<b>Frequency (GHz)</b>	210	240	275-305	165	300	217	
<b>Source Type</b>	Oscillator	Frequency Multiplier	Off-Chip	Oscillator	Frequency Multiplier	Oscillator	
<b>Output Power (dBm)</b>	4.6	0	-14.5	-1.7	-4.4	4.8 (X-pol) 4.6 (Y-pol)	
<b>EIRP (dBm)</b>	5.13	1	\	\	21.86	21.1 (X-pol) 20.9 (Y-pol)	
<b>Modulation Scheme</b>	OOK	QPSK/BPSK	32-QAM	OOK	QPSK/QAM	SO-ASK	4-Level SO-ASK
<b>Data Rate (Gb/s)</b>	$10^{(3)}$	16	$17.5 \times 6^{(4)}$	9.4	2.73	24.4 (demo) <sup>(1)</sup> $> 40$ (estimated)	16.8 (demo) <sup>(1)</sup> $> 80$ (estimated)
<b>Demonstrated Range (cm)</b>	\ <sup>(3)</sup>	1 (Wireless)	0 (Probed)	2.3 (Waveguide)	15 (Wireless)	10 <sup>(2)</sup> (Wireless)	5 <sup>(2)</sup> (Wireless)
<b>DC Power (mW)</b>	240	220	1400	6.4	1030	450×2	
<b>Area (mm<sup>2</sup>)</b>	3.5 (Chip)	2 (Chip)	6 (Chip)	0.46 (Chip)	1.7 (Chip)	0.096 (TX Cell) 2.8 (Chip)	
<b>Technology [<math>f_T / f_{max}</math> (GHz)]</b>	32nm SOI [250 / 320]	65nm CMOS [NA / NA]	40nm CMOS [NA / 280]	65nm CMOS [200 / 240]	130 nm SiGe [300 / 450]	130 nm SiGe [220 / 280]	
<b>Efficiency (pJ/bit/cm)<sup>(5)</sup></b>	\	13.8	\	\	25.2	3.7 <sup>(1,2)</sup>	
<b>Silicon Lens Used</b>	\	\	\	\	Collimating (both RX and TX)	Non-collimating	

(1) Demonstrated data rate is limited by the speed of the on-chip PRBS and thermometer encoder circuits.

(2) Demonstrated range is degraded by the 17 dB SNR drop caused by the impedance mismatch between the ZBD-F and oscilloscope.

(3) Not demonstrated, calculated from receiver bandwidth. (4) Six frequency channels combined.

(5) Efficiency =  $P_{DC} / Data\ Rate / Range$ .

oscillators takes 400 mW, the switches and data buffers dissipate 40.5 and 9.2 mW, respectively.

### C. Lens System Experiment

To further extend the communication range, Teflon lens system can be used to increase the directivity of the terahertz beam. The setup of the lens system is shown in Fig. 29(a), in which two Teflon lenses (10-cm focal length and 5-cm diameter) are used to collimate and focus the transmitted terahertz beam. For ease of alignment, the transmitter and receiver are first placed with a small distance, and then gradually moved apart with two linear tracks, as shown in Fig. 29(b). With this system, the communication range can be extended to 52 cm. With PRBS clock of 5 GHz and multi-level turned off, the measured X-polarized channel eye diagram is shown in Fig. 30(a). With PRBS clock of 1.5 GHz and multi-level turned on, the eye diagram is shown in Fig. 30(b). Theoretically, with good alignment, the range can be further extended, however, in our experiment, the largest distance is limited by the length of the linear tracks.

### V. CONCLUSION

A performance summary of the proposed SO-ASK transmitter chip as well as a comparison with other state-of-the-art works are shown in Table III. The proposed oscillator-based self-sustaining transmitter requires no additional inputs other than the input data and dc supply (e.g., high frequency LO). The return-path-gap-based self-feeding oscillators have excellent signal generation efficiency, and the high-speed constant-load switch can modulate the signal with minimum loss, consequently, the transmitter demonstrates excellent power efficiency. With the compact TX cell design, array

configuration is easily implemented to enhance the transmitter EIRP. This helps to obtain a 10-cm communication range without using any collimating lens. In [3], a transmitter efficiency is calculated by  $Eff = P_{DC} / DataRate$ , however, this fails to incorporate the communication range performance of the transmitter, which is very important in real applications. Consequently, another commonly used efficiency metric  $Eff = P_{DC} / DataRate / Range$  is calculated in Table III. Please note that this efficiency metric does not favor transmitters targeted at longer communication range ( $D$ ) like this paper, since the path loss in wireless communication increases by  $D^2$  instead of  $D$ , which means the transmitter power consumption normally needs to increase more than linearly to generate enough output power to compensate the path loss. However, even with demonstrated speed limited by the PRBS and encoder circuits as well as SNR drop caused by the receiver impedance mismatch, this paper still shows much higher transmitter efficiency.

### ACKNOWLEDGMENT

The authors would like to thank STMicroelectronics for the chip fabrication.

### REFERENCES

- [1] J. Federici and L. Moeller, "Review of terahertz and subterahertz wireless communications," *J. Appl. Phys.*, vol. 107, no. 11, p. 111101, 2010.
- [2] Z. Wang, P.-Y. Chiang, P. Nazari, C.-C. Wang, Z. Chen, and P. Heydari, "A CMOS 210-GHz fundamental transceiver with OOK modulation," *IEEE J. Solid-State Circuits*, vol. 49, no. 3, pp. 564–580, Mar. 2014.
- [3] S. Kang, S. V. Thyagarajan, and A. M. Niknejad, "A 240 GHz fully integrated wideband QPSK transmitter in 65 nm CMOS," *IEEE J. Solid-State Circuits*, vol. 50, no. 10, pp. 2256–2267, Oct. 2015.
- [4] S. V. Thyagarajan, S. Kang, and A. M. Niknejad, "A 240 GHz fully integrated wideband QPSK receiver in 65 nm CMOS," *IEEE J. Solid-State Circuits*, vol. 50, no. 10, pp. 2268–2280, Oct. 2015.

- [5] K. Katayama *et al.*, "A 300 GHz 40 nm CMOS transmitter with 32-QAM 17.5 Gb/s/ch capability over 6 channels," in *Proc. IEEE Int. Solid-State Circuits Conf. (ISSCC) Dig. Tech. Papers*, Jan. 2016, pp. 342–343.
- [6] E. Afshari and R. Han, "Progress towards mW-power generation in CMOS THz signal sources," in *Proc. 8th Eur. Microw. Integr. Circuits Conf. (EuMIC)*, Oct. 2013, pp. 117–120.
- [7] C. Jiang, A. Cathelin, and E. Afshari, "An efficient 210 GHz compact harmonic oscillator with 1.4 dBm peak output power and 10.6% tuning range in 130 nm BiCMOS," in *Proc. IEEE Radio Freq. Integr. Circuits Symp.*, May 2016, pp. 194–197.
- [8] J. D. Jackson, *Classical Electrodynamics*. 3rd ed. Hoboken, NJ, USA: Wiley, 1979.
- [9] S. Haykin, *Digital Communications*. Hoboken, NJ, USA: Wiley, 1998.
- [10] J. F. Wakerly, *Digital Design: Principles and Practices*. Englewood Cliffs, NJ, USA: Prentice-Hall, 1994.
- [11] C. Jiang *et al.*, "A 320 GHz subharmonic-mixing coherent imager in 0.13  $\mu$ m SiGe BiCMOS," in *Proc. IEEE Int. Solid-State Circuits Conf. (ISSCC) Dig. Tech. Papers*, Jan. 2016, pp. 432–434.
- [12] Q. Zhong, W. Choi, C. Miller, R. Henderson, and K. K. O, "A 210-to-305 GHz CMOS receiver for rotational spectroscopy," in *Proc. IEEE Int. Solid-State Circuits Conf. (ISSCC) Dig. Tech. Papers*, Jan. 2016, pp. 426–427.
- [13] P. Chevalier *et al.*, "Scaling of SiGe BiCMOS technologies for applications above 100 GHz," in *Proc. IEEE Compound Semiconductor Integr. Circuit Symp.*, Oct. 2012, pp. 1–4.
- [14] R. Han *et al.*, "A SiGe terahertz heterodyne imaging transmitter with 3.3 mW radiated power and fully-integrated phase-locked loop," *IEEE J. Solid-State Circuits*, vol. 50, no. 12, pp. 2935–2947, Dec. 2015.
- [15] D. M. Pozar, *Microwave Engineering*. New York, NY, USA: Wiley, 2005.
- [16] T. Hirota, A. Minakawa, and M. Muraguchi, "Reduced-size branch-line and rat-race hybrids for uniplanar MMIC's," *IEEE Trans. Microw. Theory Tech.*, vol. 38, no. 3, pp. 270–275, Mar. 1990.
- [17] R. Han and E. Afshari, "A CMOS high-power broadband 260-GHz radiator array for spectroscopy," *IEEE J. Solid-State Circuits*, vol. 48, no. 12, pp. 3090–3104, Dec. 2013.
- [18] *Nominal Horn Specification*, Virginia Diodes, Inc., Charlottesville, VA, USA, 2016.
- [19] C. A. Balanis, *Antenna Theory: Analysis and Design*. Hoboken, NJ, USA: Wiley, 2015.
- [20] H. T. Friis, "A note on a simple transmission formula," *Proc. IRE*, vol. 34, no. 5, pp. 254–256, May 1946.
- [21] *WR5.IZBD-F User Guide*, Virginia Diodes, Inc., Charlottesville, VA, USA, 2016.
- [22] *Agilent 83483A,4A,4B and 54751A,2A,2B Plug-In Modules User's Guide*, Agilent Technologies, Santa Clara, CA, USA, 2000.
- [23] B. Razavi, *RF Microelectronics*, 2nd ed. Englewood Cliffs, NJ, USA: Prentice-Hall, 2011.
- [24] M. Uzunkol, O. D. Gurbuz, F. Golcuk, and G. M. Rebeiz, "A 0.32 THz SiGe 4×4 imaging array using high-efficiency on-chip antennas," *IEEE J. Solid-State Circuits*, vol. 48, no. 9, pp. 2056–2066, Sep. 2013.
- [25] K. Sengupta, D. Seo, L. Yang, and A. Hajimiri, "Silicon integrated 280 GHz imaging chipset with 4 × 4 SiGe receiver array and CMOS source," *IEEE Trans. Terahertz Sci. Technol.*, vol. 5, no. 3, pp. 427–437, May 2015.
- [26] R. Han *et al.*, "Active terahertz imaging using Schottky diodes in CMOS: Array and 860-GHz pixel," *IEEE J. Solid-State Circuits*, vol. 48, no. 10, pp. 2296–2308, Oct. 2013.
- [27] H.-J. Song, J.-Y. Kim, K. Ajito, N. Kukutsu, and M. Yaita, "50-Gb/s direct conversion QPSK modulator and demodulator MMICs for terahertz communications at 300 GHz," *IEEE Trans. Microw. Theory Tech.*, vol. 62, no. 3, pp. 600–609, Mar. 2014.
- [28] Y. Ye, B. Yu, and Q. J. Gu, "A 165-GHz transmitter with 10.6% peak DC-to-RF efficiency and 0.68-pJ/b energy efficiency in 65-nm bulk CMOS," *IEEE Trans. Microw. Theory Tech.*, vol. 64, no. 12, pp. 4573–4584, Dec. 2016.
- [29] N. Sarmah *et al.*, "A fully integrated 240-GHz direct-conversion quadrature transmitter and receiver chipset in SiGe technology," *IEEE Trans. Microw. Theory Tech.*, vol. 64, no. 2, pp. 562–574, Feb. 2016.
- [30] J.-D. Park, S. Kang, S. V. Thyagarajan, E. Alon, and A. M. Niknejad, "A 260 GHz fully integrated CMOS transceiver for wireless chip-to-chip communication," in *Proc. IEEE Symp. (VLSI Circuits)*, Jun. 2012, pp. 48–49.
- [31] O. Momeni and E. Afshari, "High power terahertz and millimeter-wave oscillator design: A systematic approach," *IEEE J. Solid-State Circuits*, vol. 46, no. 3, pp. 583–597, Mar. 2011.
- [32] C. Jiang *et al.*, "A fully integrated 320 GHz coherent imaging transceiver in 130 nm SiGe BiCMOS," *IEEE J. Solid-State Circuits*, vol. 51, no. 11, pp. 2596–2609, Nov. 2016.
- [33] M. Adnan and E. Afshari, "A 247-to-263.5 GHz VCO with 2.6 mW peak output power and 1.14% DC-to-RF efficiency in 65 nm bulk CMOS," in *Proc. ISSCC Dig. Tech. Papers*, Feb. 2014, pp. 262–263.
- [34] S. Jameson, E. Halpern, and E. Socher, "A 300 GHz wirelessly locked 2 × 3 array radiating 5.4 dBm with 5.1% DC-to-RF efficiency in 65 nm CMOS," *Proc. ISSCC Dig. Tech. Papers*, Feb. 2016, pp. 348–349.
- [35] M. Elkhouly, Y. Mao, C. Meliani, F. Ellinger, and C. Schyett, "A 245 GHz ASK modulator and demodulator with 40 Gbits/sec data rate in 0.13  $\mu$ m SiGe BiCMOS technology," in *Proc. IEEE Int. Microw. Symp. (IMS)*, Jun. 2013, pp. 1–3.



**Chen Jiang** (S'15) received the B.Sc. and M.Sc. degree in Microelectronics from Fudan University, Shanghai, China, in 2010 and 2013, respectively, the M.Sc. degree in Electrical and Computer Engineering from Cornell University, Ithaca, NY, USA, in 2016. Currently, he is working towards the Ph.D. degree at Cornell University. In September 2016, he joined the Radiation Laboratory at University of Michigan, Ann Arbor, as a visiting student. His major research focus is novel millimeter-wave and terahertz electronics for imaging, sensing and communication applications.

Mr. Jiang is a member of the IEEE Solid-State Circuits Society and the IEEE Microwave Theory and Techniques Society. He was the recipient of the Irwin and Joan Jacobs Fellowship, Cornell University, in 2013, the Sporck Analog Design Fellowship, Cornell University, in 2014, the IEEE Solid-State Circuits Society Predoctoral Achievement Award and the IEEE Microwave Theory and Techniques Society Graduate Fellowship in 2017.



**Andreia Cathelin** (M'04–SM'11) started her electronic studies at the Polytechnic Institute of Bucharest, Romania, and graduated from the Institut Supérieur d'Électronique du Nord (ISEN), Lille, France, in 1994. In 1998 and 2013, respectively, she received the Ph.D. and "habilitation à diriger des recherches" (French highest academic degree) degrees from the Université de Lille 1, France.

In 1997, she was with Info Technologies, Grignan, France, working on analog and RF communications design. Since 1998, she has been with STMicroelectronics, Crolles, France, now in the Embedded Processing Solutions Segment, Technology R&D, as a Senior Member of the Technical Staff. Her major fields of interest are in the area of RF/mmW/THz systems for communications and imaging. She has authored or co-authored 100 technical papers and 4 book chapters, and has filed more than 25 patents.

Dr. Cathelin is serving on several IEEE conferences and committees. She has been active at ISSCC since 2011. In 2011, she was a TPC member, the RF sub-committee chair from 2012 to 2015, and is now Forums Chair and member of the Executive Committee. She is a member of several Technical Program Committees: VLSI Symposium on Circuits since 2010, currently serving as officer and ESSCIRC since 2005. Since September 2013, she has been on the Steering Committee of the ESSCIRC-ESSDERC conferences, currently serving as Vice-Chair. She is a well member of the experts' team of the AERES (French Evaluation Agency for Research and Higher Education). She is a co-recipient of the ISSCC 2012 Jan Van Vessem Award for Outstanding European Paper and of the ISSCC 2013 Jack Kilby Award for Outstanding Student Paper, as well as winner of the 2012 STMicroelectronics Technology Council Innovation Prize. She is an elected member of the IEEE SSCS Adcom for the term January 2015 to December 2017.



**Ehsan Afshari** (S'98–M'07–SM'11) was born in 1979. He received the B.Sc. degree in Electronics Engineering from the Sharif University of Technology, Tehran, Iran and the M.S. and Ph.D. degree in Electrical Engineering from the California Institute of Technology, Pasadena, in 2003, and 2006, respectively. In August 2006, he joined the faculty in Electrical and Computer Engineering at Cornell University as an Assistant Professor, and was promoted to Associate Professor in 2012. In Fall 2016, he joined the Electrical Engineering and Computer Science department at The University of Michigan at Ann Arbor, as an Associate Professor. His research interests are mm-wave and terahertz electronics and low-noise integrated circuits for applications in communication systems, sensing, and biomedical devices.

Prof. Afshari serves as the Distinguished Lecturer of the IEEE Solid-State Circuits Society and a member of the Technical Program Committee of the IEEE Radio Frequency Integrated Circuits Symposium (RFIC). He was the

chair of the IEEE Ithaca section, the chair of Cornell Highly Integrated Physical Systems (CHIPS), a member of International Technical Committee of the IEEE Solid-State Circuit Conference (ISSCC), a member of the Analog Signal Processing Technical Committee of the IEEE Circuits and Systems Society, a member of the Technical Program Committee of the IEEE Custom Integrated Circuits Conference (CICC), and a member of Technical Program Committee of the IEEE International Conference on Ultra-Wideband (ICUWB). He was awarded National Science Foundation CAREER award in 2010, Cornell College of Engineering Michael Tien excellence in teaching award in 2010, Defense Advanced Research Projects Agency (DARPA) Young Faculty Award in 2008, and Iran's Best Engineering Student award by the President of Iran in 2001. He is also the recipient of the best paper award in the Custom Integrated Circuits Conference (CICC), September 2003, the first place at Stanford-Berkeley-Caltech Inventors Challenge, March 2005, the best undergraduate paper award in Iranian Conference on Electrical Engineering, 1999, the recipient of the Silver Medal in the Physics Olympiad in 1997, and the recipient of the Award of Excellence in Engineering Education from Association of Professors and Scholars of Iranian Heritage (APSIH), May 2004.